Journal of the Optical Society of America B
OPTICAL PHYSICS

Multiple electromagnetically induced grating in the ^{85}Rb five-level atomic medium

Nguyen Thi Quynh Anh,[1] Nguyen Huy Bang,[1,2] Ha Thi Quynh Anh,[1] Truong Chu Van Anh,[1] Ngo Thi Tuyet Mai,[1] Nguyen Thi Nhung,[1] Trinh Thi Nhu,[1] Le Tra My,[1] Le Thi Minh Huyen,[1] Ngo Tien Hung,[1] and Le Van Doai[1,*]

[1]Vinh University, 182 Le Duan Street, Vinh City, Vietnam
[2]bangnh@vinhuni.edu.vn
*doailv@vinhuni.edu.vn

Received 8 January 2024; revised 23 February 2024; accepted 7 March 2024; posted 7 March 2024; published 19 March 2024

In this work, a multiple electromagnetically induced grating is realized based on multiple electromagnetically induced transparency in the ^{85}Rb five-level atomic medium. We demonstrate that the diffraction pattern of the probe light field is observed at three different frequency regions corresponding to the three transparent spectral regions of the system. The influence of the intensity and frequency of the coupling laser field on the diffraction pattern of the electromagnetically induced grating and its diffraction efficiency is also investigated, which can find the optimal parameters to improve the higher-order diffraction efficiencies. The appearance of the multiple electromagnetically induced grating in multi-level atomic systems can be applied to photonic devices operating with multiple frequency channels.

https://doi.org/10.1364/JOSAB.517939

1. INTRODUCTION

Coherent interaction between laser fields with an atom can lead to a quantum interference of transition probabilities within the atomic system. As a result, it suppresses (destructive interference) or enhances (constructive interference) the total transition probability and thus significantly changes the absorption or transmission properties of the atomic medium for a light field. The constructive interference of transition probabilities can generate electromagnetically induced transparency (EIT) [1,2], while the destructive interference can lead to electromagnetically induced absorption (EIA) [3]. In the presence of EIT, the atomic medium exhibits unique optical properties [2], which have enabled novel potential applications such as lasing without inversion [4], giant nonlinearity [5,6], low threshold optical bistability [7], slow and storage light [8,9], lossless propagation of a light pulse and all-optical switching [10,11], electromagnetically induced grating (EIG) [12,13], and so on.

The simplest model of EIT is a three-level atomic system excited by a probe laser field and a coupling laser field according to lambda, cascade, and V configurations [2]. However, three-level atomic configurations are limited to one EIT window on the absorption profile. This is a reason of prompting research towards multi-level atomic systems capable of exhibiting multi-EIT (MEIT) at distinct atomic transitions [14–18]. These advanced multi-EIT systems unveil promising applications, including multi-frequency slow light [17–19], multi-frequency enhanced Kerr nonlinearity [20], multi-frequency optical bistability [21], controllable entanglements [22], etc. Conventionally, achieving MEIT demanded multiple coupling laser fields alongside the probe field, resulting in complex manipulation between EIT windows [2]. However, recent advancements have demonstrated the generation of MEIT using only one coupling field by taking advantage of closely spaced hyperfine states in multi-level atomic systems [23]. This experiment was performed in the five-level configuration of the ^{85}Rb atom, and three EIT windows were observed [23]. Subsequent development of an analytical model yielded excellent agreement with experimental results [24]. The foremost notable advantage of this model is that three EIT windows are created simultaneously with only one coupling field while the manipulation of the EIT windows is also facilitated by adjusting only one coupling field. Recently, this MEIT property of the five-level ladder atomic system has also been applied to simply realize multi-frequency slow light [25], multi-frequency giant Kerr nonlinearity [26], as well as multi-frequency optical bistability [27].

On the other hand, by replacing the traveling wave coupling field in the EIT by a standing wave field, an electromagnetically induced grating is formed [12,13]. In the presence of a standing wave coupling field, it will cause in space a periodic modulation of the transmitted spectrum of the probe field. That is, the probe field propagates through the atomic sample just as it passes through a diffraction grating. As a result, the probe field can be diffracted into the high-order directions. So far, theoretical

and experimental studies of EIG have attracted great attention [28–32] due to its potential applications in many fields, such as atomic velocimetry [33], realizing optical bistability [34], all-optical switching and routing [35], light storage [36], beam splitting and fanning [37], shaping a biphoton spectrum [38], modern photonic devices [39], controlling multi-wave mixing processes [40], angular Talbot effect [41], and giant Goos–Hänchen shifts [42].

The early studies on EIT-based EIG in three-level atomic systems demonstrated that the probe field can be diffracted into the high-order directions and high diffraction efficiencies were achieved. Recent researches have witnessed significant enhancement in EIG efficiency within diverse four-level atomic systems aided by other external fields such as a microwave field [43,44] and magnetic field [45] as well as coherence effects such as coherent population trapping (CPT) [46], Kerr nonlinearity [47,48], and spontaneously generated coherence (SGC) [47–49]. The studies in these works demonstrated energy transfer from zero-order diffraction to higher-order diffractions by the added external field. However, such studies have not yet demonstrated the generation of multi-EIG (MEIG) at different frequencies of laser fields. Very recently, Lu Zhao realized an electromagnetically induced polarization grating in a degenerate five-level $\Xi-\Lambda$ system under an external magnetic field and showed that the two circularly polarized $\sigma^{\pm}$ components of the probe field can be decoupled and flexibly controlled by diffraction, thus generating a plurality of purely polarized beams at different angles in one and two dimensions in the far field [50]. Vafafard and Sahrai [51] demonstrated that a double electromagnetically induced grating can be generated in a tripod four-level atomic system with both the probe and signal fields at two different frequency detunings due to the presence of an incoherent pump field.

Although multiple electromagnetically induced transparency has been demonstrated in some multi-level atomic systems [17,18,23,24,52], a similar study for a multiple electromagnetically induced grating is still very modest. In this work, we use the MEIT property of a five-level atomic system to realize MEIG. For the first time, the diffraction pattern of the probe field is obtained simultaneously at three different frequency regions corresponding to three EIT windows of the system. The influence of the intensity and frequency of the laser fields on the diffraction patterns of the EIG as well as the diffraction efficiency was also investigated. This study paves the way for exciting applications of MEIG analogous to those of MEIT.

2. THEORETICAL MODEL

The five-level ladder-type atomic system excited by a probe laser field and only one coupling laser field is shown in Fig. 1(a). The weak probe field with frequency ω_p is applied to the transition $|1\rangle \leftrightarrow |2\rangle$, whereas the intense coupling field with frequency ω_c is coupled simultaneously to the transitions from the level $|2\rangle$ to three hyperfine levels $|3\rangle$, $|4\rangle$, and $|5\rangle$. We assume that the probe field is a traveling wave propagating along the z-direction and represented by $\varepsilon_p = \frac{1}{2}E_p e^{-i\omega_p t+ik_p z} + \text{c.c.}$, where E_p is assumed to be unchanged along the x-direction and the wave vector $k_p = \frac{2\pi}{\lambda_p}$ with λ_p is the wavelength of the probe laser field. Meanwhile, the coupling field is the standing wave and is

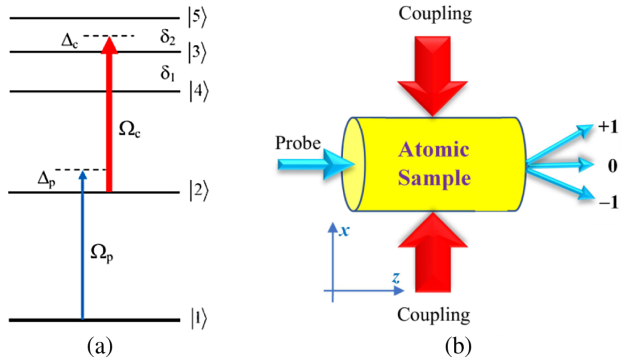

Fig. 1. (a) Five-level ladder-type atomic system excited by a probe laser field and only one coupling laser field. (b) Orientations of probe and coupling laser fields propagating through the atomic sample.

expressed by $\varepsilon_c = \frac{1}{2}E_c \sin(k_{cx}x)e^{-i\omega_c t+ik_{cz}z} + \text{c.c.}$, where E_c is taken as the constant amplitude factor, and the wave vector $\vec{k}_c = k_{cx}\hat{x} + k_{cz}\hat{z}$ with k_{cx} can be written as $k_{cx} = \frac{2\pi \sin\phi}{\lambda_c} \equiv \frac{\pi}{\Lambda}$, and $\Lambda = \frac{\lambda_c}{2\sin\phi}$ denotes the separation between two consecutive nodes or antinodes, λ_c is the wavelength of the coupling field, and ϕ is the angle made by the direction of the coupling field to the direction of the probe field propagating towards the z-axis. By changing the angle ϕ, the value of Λ can be varied. Figure 1(b) indicates the propagation of probe and coupling fields through the atomic sample.

Semi-classical theory can be used to describe the interaction between the atom and laser fields. The total Hamiltonian H is the sum of the unperturbed atomic Hamiltonian H_{at} and the interaction Hamiltonian H_{int}, is given by

$$\begin{aligned} H = &\sum_{n=1}^{5} \hbar\omega_n |n\rangle\langle n| + \Omega_p e^{-i\omega_p t+ik_p z}|1\rangle\langle 2| \\ &+ \Omega_c \sin\left(\frac{\pi x}{\Lambda}\right) e^{-i\omega_c t+ik_{cz}z} (a_{32}|2\rangle\langle 3| + a_{42}|2\rangle\langle 4| \\ &+ a_{52}|2\rangle\langle 5|) + \text{c.c}, \end{aligned} \tag{1}$$

where $\Omega_p = d_{21}E_p/\hbar$ and $\Omega_c = d_{32}E_c/\hbar$ are Rabi frequencies induced by the probe and coupling laser fields, respectively; $a_{32} = d_{32}/d_{32}$, $a_{42} = d_{42}/d_{32}$, and $a_{52} = d_{52}/d_{32}$ are the coupling strengths of the transitions from the level $|2\rangle$ to the hyperfine levels $|3\rangle$, $|4\rangle$, and $|5\rangle$.

In laser fields, the time evolution of atomic states that are represented by the density matrix ρ is obeyed by the following Liouville equation:

$$\dot{\rho} = -\frac{i}{\hbar}[H, \rho] + \Gamma\rho, \tag{2}$$

where the term $\Gamma\rho$ presents the relaxation mechanisms of the system.

From Eqs. (1) and (2) and using electric-dipole and rotating-wave approximations, the density matrix equations representing the atomic population and coherence are expressed as [24]

$$\dot{\rho}_{55} = -\Gamma_{52}\rho_{55} - \frac{i}{2}a_{52}\Omega_c \sin\left(\frac{\pi x}{\Lambda}\right)(\rho_{25} - \rho_{52}), \tag{3a}$$

$$\dot{\rho}_{44} = -\Gamma_{42}\rho_{44} - \frac{i}{2}a_{42}\Omega_c \sin\left(\frac{\pi x}{\Lambda}\right)(\rho_{24} - \rho_{42}), \tag{3b}$$

$$\dot{\rho}_{33} = -\Gamma_{32}\rho_{33} - \frac{i}{2}a_{32}\Omega_c \sin\left(\frac{\pi x}{\Lambda}\right)(\rho_{23} - \rho_{32}), \tag{3c}$$

$$\begin{aligned}\dot{\rho}_{22} = &-\Gamma_{21}\rho_{22} + \Gamma_{32}\rho_{33} + \Gamma_{42}\rho_{44} + \Gamma_{52}\rho_{55} - \frac{i}{2}\Omega_p(\rho_{12} - \rho_{21}) \\ &- \frac{i}{2}a_{32}\Omega_c \sin\left(\frac{\pi x}{\Lambda}\right)(\rho_{32} - \rho_{23}) \\ &- \frac{i}{2}a_{42}\Omega_c \sin\left(\frac{\pi x}{\Lambda}\right)(\rho_{42} - \rho_{24}) \\ &- \frac{i}{2}a_{52}\Omega_c \sin\left(\frac{\pi x}{\Lambda}\right)(\rho_{52} - \rho_{25}),\end{aligned} \tag{3d}$$

$$\dot{\rho}_{11} = \Gamma_{21}\rho_{22} - \frac{i}{2}\Omega_p(\rho_{21} - \rho_{12}), \tag{3e}$$

$$\begin{aligned}\dot{\rho}_{54} = &-[i(\delta_1 + \delta_2) + \gamma_{54}]\rho_{54} + \frac{i}{2}a_{42}\Omega_c \sin\left(\frac{\pi x}{\Lambda}\right)\rho_{52} \\ &- \frac{i}{2}a_{52}\Omega_c \sin\left(\frac{\pi x}{\Lambda}\right)\rho_{24},\end{aligned} \tag{3f}$$

$$\begin{aligned}\dot{\rho}_{53} = &-(i\delta_2 + \gamma_{53})\rho_{53} + \frac{i}{2}a_{32}\Omega_c \sin\left(\frac{\pi x}{\Lambda}\right)\rho_{52} \\ &- \frac{i}{2}a_{52}\Omega_c \sin\left(\frac{\pi x}{\Lambda}\right)\rho_{23},\end{aligned} \tag{3g}$$

$$\begin{aligned}\dot{\rho}_{52} = &[i(\Delta_c - \delta_2) - \gamma_{52}]\rho_{52} + \frac{i}{2}\Omega_p\rho_{51} + \frac{i}{2}a_{32}\Omega_c \sin\left(\frac{\pi x}{\Lambda}\right)\rho_{53} \\ &+ \frac{i}{2}a_{42}\Omega_c \sin\left(\frac{\pi x}{\Lambda}\right)\rho_{54} + \frac{i}{2}a_{52}\Omega_c \sin\left(\frac{\pi x}{\Lambda}\right)[\rho_{55} - \rho_{22}],\end{aligned} \tag{3h}$$

$$\begin{aligned}\dot{\rho}_{51} = &\left[i\left(\Delta_c + \Delta_p - \delta_2\right) - \gamma_{51}\right]\rho_{51} \\ &+ \frac{i}{2}\Omega_p\rho_{52} - \frac{i}{2}a_{52}\Omega_c \sin\left(\frac{\pi x}{\Lambda}\right)\rho_{21},\end{aligned} \tag{3i}$$

$$\begin{aligned}\dot{\rho}_{43} = &-[i\delta_1 + \gamma_{43}]\rho_{43} - \frac{i}{2}a_{42}\Omega_c \sin\left(\frac{\pi x}{\Lambda}\right)\rho_{23} \\ &+ \frac{i}{2}a_{32}\Omega_c \sin\left(\frac{\pi x}{\Lambda}\right)\rho_{42},\end{aligned} \tag{3j}$$

$$\begin{aligned}\dot{\rho}_{42} = &[i(\Delta_c + \delta_1) - \gamma_{42}]\rho_{42} + \frac{i}{2}\Omega_p\rho_{41} + \frac{i}{2}a_{32}\Omega_c \sin\left(\frac{\pi x}{\Lambda}\right)\rho_{43} \\ &+ \frac{i}{2}a_{52}\Omega_c \sin\left(\frac{\pi x}{\Lambda}\right)\rho_{45} + \frac{i}{2}a_{42}\Omega_c \sin\left(\frac{\pi x}{\Lambda}\right)(\rho_{44} - \rho_{22}),\end{aligned} \tag{3k}$$

$$\begin{aligned}\dot{\rho}_{41} = &\left[i(\Delta_c + \Delta_p + \delta_1) - \gamma_{41}\right]\rho_{41} + \frac{i}{2}\Omega_p\rho_{42} \\ &- \frac{i}{2}a_{42}\Omega_c \sin\left(\frac{\pi x}{\Lambda}\right)\rho_{21},\end{aligned} \tag{3l}$$

$$\begin{aligned}\dot{\rho}_{32} = &(i\Delta_c - \gamma_{32})\rho_{32} + \frac{i}{2}\Omega_p\rho_{31} + \frac{i}{2}a_{42}\Omega_c \sin\left(\frac{\pi x}{\Lambda}\right)\rho_{34} \\ &+ \frac{i}{2}a_{52}\Omega_c \sin\left(\frac{\pi x}{\Lambda}\right)\rho_{35} + \frac{i}{2}a_{32}\Omega_c \sin\left(\frac{\pi x}{\Lambda}\right)(\rho_{33} - \rho_{22}),\end{aligned} \tag{3m}$$

$$\dot{\rho}_{31} = \left[i(\Delta_c + \Delta_p) - \gamma_{31}\right]\rho_{31} + \frac{i}{2}\Omega_p\rho_{32} - \frac{i}{2}a_{32}\Omega_c \sin\left(\frac{\pi x}{\Lambda}\right)\rho_{21}, \tag{3n}$$

$$\begin{aligned}\dot{\rho}_{21} = &\left(i\Delta_p - \gamma_{21}\right)\rho_{21} \\ &- \frac{i}{2}a_{32}\Omega_c \sin\left(\frac{\pi x}{\Lambda}\right)\rho_{31} - \frac{i}{2}a_{42}\Omega_c \sin\left(\frac{\pi x}{\Lambda}\right)\rho_{41} \\ &- \frac{i}{2}a_{52}\Omega_c \sin\left(\frac{\pi x}{\Lambda}\right)\rho_{51} + \frac{i}{2}\Omega_p(\rho_{22} - \rho_{11}),\end{aligned} \tag{3o}$$

where $\Delta_p = \omega_p - \omega_{21}$ and $\Delta_c = \omega_c - \omega_{32}$ denote the frequency detunings of the probe and coupling lasers, respectively; δ_1 and δ_2 are frequency separations between the levels $|3\rangle - |4\rangle$ and $|5\rangle - |3\rangle$, respectively; Γ_{mn} is the decay rate from the upper state $|n\rangle$ to the lower state $|m\rangle$, while γ_{mn} is the relaxation rate of atomic coherence ρ_{mn}.

Under the weak field approximation, we assume that initially the atom is in the ground state $|1\rangle$, $\rho_{11}^{(0)} \approx 1$ while $\rho_{22}^{(0)} \approx \rho_{33}^{(0)} \approx \rho_{44}^{(0)} \approx \rho_{55}^{(0)} \approx 0$. We analytically solve the density matrix Eq. (3) in the steady state to find the off-diagonal density matrix element ρ_{21} corresponding to the response of the medium to the probe field. The result obtained is as follows [24]:

$$\rho_{21} = \frac{\frac{i}{2}\Omega_p\left(\rho_{22}^{(0)} - \rho_{11}^{(0)}\right)}{F}, \tag{4a}$$

$$\begin{aligned}F = &\gamma_{21} - i\Delta_p + \frac{(a_{32}\Omega_c/2)^2 \sin^2\left(\frac{\pi x}{\Lambda}\right)}{\gamma_{31} - i(\Delta_p + \Delta_c)} \\ &+ \frac{(a_{42}\Omega_c/2)^2 \sin^2\left(\frac{\pi x}{\Lambda}\right)}{\gamma_{41} - i(\Delta_p + \Delta_c + \delta_1)} + \frac{(a_{52}\Omega_c/2)^2 \sin^2\left(\frac{\pi x}{\Lambda}\right)}{\gamma_{51} - i(\Delta_p + \Delta_c - \delta_2)}.\end{aligned} \tag{4b}$$

It is well known that the response of the atomic medium to the probe field is governed by its polarization $P = Nd_{21}\rho_{21} \equiv \frac{1}{2}\varepsilon_0\chi E_p$; thus, the probe susceptibility is given by

$$\chi = 2\frac{Nd_{21}}{\varepsilon_0 E_p}\rho_{21} = \frac{Nd_{21}^2}{\varepsilon_0\hbar}\left(\frac{A}{A^2 + B^2} + i\frac{B}{A^2 + B^2}\right), \tag{5}$$

with N being the atomic density, and A and B are real parameters as

$$A = -\Delta_p + \frac{A_{32}}{\gamma_{31}} + \frac{A_{42}}{\gamma_{41}} + \frac{A_{52}}{\gamma_{51}}, \tag{6a}$$

$$B = \gamma_{21} + \frac{A_{32}}{\Delta_p + \Delta_c} + \frac{A_{42}}{\Delta_p + \Delta_c + \delta_1} + \frac{A_{52}}{\Delta_p + \Delta_c - \delta_2}, \tag{6b}$$

$$A_{32}=\frac{\gamma_{31}(\Delta_p+\Delta_c)}{\gamma_{31}^2+(\Delta_p+\Delta_c)^2}\left[\frac{a_{32}\Omega_c\sin\left(\frac{\pi x}{\Lambda}\right)}{2}\right]^2, \tag{7a}$$

$$A_{42}=\frac{\gamma_{41}(\Delta_p+\Delta_c+\delta_1)}{\gamma_{41}^2+(\Delta_p+\Delta_c+\delta_1)^2}\left[\frac{a_{42}\Omega_c\sin\left(\frac{\pi x}{\Lambda}\right)}{2}\right]^2, \tag{7b}$$

$$A_{52}=\frac{\gamma_{51}(\Delta_p+\Delta_c-\delta_2)}{\gamma_{51}^2+(\Delta_p+\Delta_c-\delta_2)^2}\left[\frac{a_{52}\Omega_c\sin\left(\frac{\pi x}{\Lambda}\right)}{2}\right]^2. \tag{7c}$$

From Eq. (5), the real $\mathrm{Re}(\chi)$ and imaginary $\mathrm{Im}(\chi)$ parts of the susceptibility are obtained as [24]

$$\mathrm{Re}(\chi)=\frac{Nd_{21}^2}{\varepsilon_0\hbar}\frac{A}{A^2+B^2}, \tag{8a}$$

$$\mathrm{Im}(\chi)=\frac{Nd_{21}^2}{\varepsilon_0\hbar}\frac{B}{A^2+B^2}. \tag{8b}$$

In order to describe the diffraction pattern of the probe field in the atomic sample, we begin with the Maxwell equation. Suppose that the probe field is propagating along the z-direction through the atomic sample of length L. In the slowly varying envelope approximation, the Maxwell equation with the atomic polarization is

$$\frac{\partial\varepsilon_p}{\partial z}=i\frac{\pi}{\varepsilon_0\lambda_p}P. \tag{9}$$

Using the expression of induced polarization $P=Nd_{21}\rho_{21}\equiv\frac{1}{2}\varepsilon_0\chi E_p$, Eq. (9) can be written as

$$\frac{\partial\varepsilon_p}{\partial z'}=i\chi\varepsilon_p, \tag{10}$$

where $z'=(\pi Nd_{21}^2/2\varepsilon_0\hbar\lambda_p)z$ and z' can be made dimensionless when $z_0=2\varepsilon_0\hbar\lambda_p/\pi Nd_{21}^2$ is taken as the unit for z. If we consider z to be the effective length L traversed by the probe field through the atomic medium, then the normalized transmission function can be written as

$$T(x)=e^{-\mathrm{Im}(\chi)L}e^{i\mathrm{Re}(\chi)L}, \tag{11}$$

where the terms $e^{-\mathrm{Im}(\chi)L}$ and $e^{i\mathrm{Re}(\chi)L}$ are associated with absorption and phase modulations, respectively. Owing to the existence of the standing wave coupling field, the transmission function for the probe field is spatially modulated. The Fraunhofer diffraction equation can be obtained by calculating the Fourier transformation of $T(x)$:

$$I_p(\theta)=|F(\theta)|^2.\frac{\sin^2(M\pi\sin(\theta)R)}{M^2\sin^2(\pi\sin(\theta)R)}, \tag{12}$$

$$F(\theta)=\int_0^1 T(x)\exp(-2i\pi x.\sin(\theta)R)\mathrm{d}x, \tag{13}$$

where $R=\Lambda/\lambda_p$, the angle θ is the diffraction angle of the probe field with regard to the z-direction, and the parameter M is introduced as the spatial width of the probe beam. The intensity of the k-order diffraction maximum is determined by using the grating equation $k=R\sin\theta$. The k-order diffraction intensity of the grating is expressed by

$$I_p(\theta_k)=|F(\theta_k)|^2\equiv\left|\int_0^1 T(x)\exp(-i2k\pi x)\mathrm{d}x\right|^2, \tag{14}$$

where $k=0$, 1, 2, corresponding to the zero-, first-, second-order diffraction intensities, respectively.

3. RESULTS AND DISCUSSION

In general, our model is applicable to many different atomic/molecular systems; as an illustrative case we apply the theoretical model to the ^{85}Rb atom with states $|1\rangle=|5S_{1/2}\,F=3\rangle$, $|2\rangle=5|P_{1/2}\,F=3\rangle$, $|3\rangle=5|D_{5/2}\,F=3\rangle$, $|4\rangle=5|D_{5/2}\,F=4\rangle$, and $|5\rangle=5|D_{5/2}\,F=2\rangle$, and the frequency gaps between the levels $|3\rangle-|4\rangle$ and between the levels $|3\rangle-5|\rangle$ are $\delta_1=9$ MHz and $\delta_2=7.6$ MHz, respectively. The atomic parameters are [23,24]: $N=4.5\times10^{17}$ atoms/m^3, $\gamma_{21}=\gamma_{23}=5.3$ MHz, $d_{21}=1.6\times10^{-29}$ C.m, and $a_{42}:a_{32}:a_{52}=1.46:1:0.6$. For simplicity, all quantities related to frequency are given in units γ, which should be on the order of MHz for rubidium atoms.

We already know that this five-level atomic configuration represents the probe field response with three EIT windows as shown in Fig. 2 [23,24]. It is specific as follows: when the coupling laser frequency is fixed at the resonant transition $|2\rangle\leftrightarrow|3\rangle$ (i.e., $\Delta_c=0$) while the probe beam scans around the transition $|1\rangle\leftrightarrow|2\rangle$, then three EIT windows appear at frequency detunings $\Delta_p=0$, $\Delta_p=-9\gamma$ and $\Delta_p=7.6\gamma$. On the other hand, if the probe laser frequency is fixed at the resonant transition $|1\rangle\leftrightarrow|2\rangle$ (i.e., $\Delta_p=0$) and the coupling beam scans around the transition $|2\rangle\leftrightarrow|3\rangle$, the EIT effect (for the probe field) occurs only when the coupling detuning is satisfied as $\Delta_c=0$, $\Delta_c=-9\gamma$ or $\Delta_c=7.6\gamma$.

We first investigate the dependence of the grating effect on the probe laser intensity in the presence of EIT as presented in Fig. 3. It shows that the optimal value range of the probe laser intensity for the diffraction pattern is in the range of 0.5γ to 1.0γ, while the grating effect disappears when the probe laser intensity is greater than 2γ.

We now demonstrate the appearance of MEIG in this system. Indeed, in Fig. 4 we plot the three-dimensional diffraction

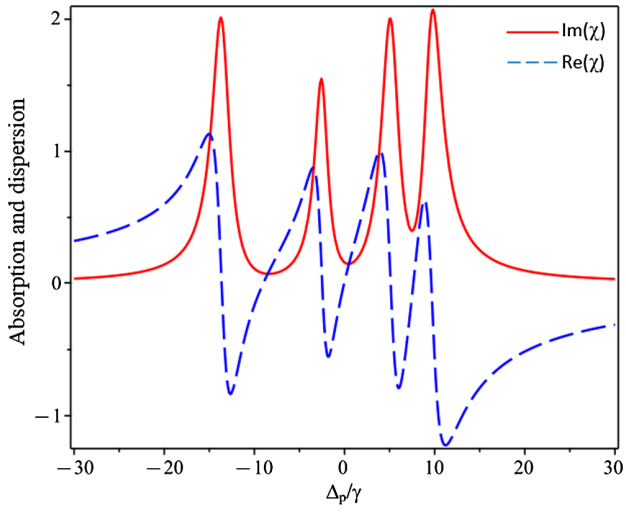

Fig. 2. Absorption (solid line) and dispersion (dashed line) versus the probe detuning when $\Delta_c=0$ and $\Omega_c=10\gamma$.

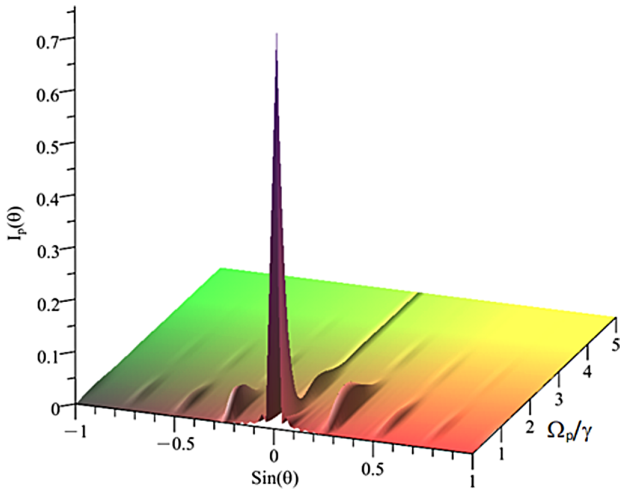

Fig. 3. Diffraction pattern as a function of sin θ and probe intensity Ω_p when the coupling intensity $\Omega_c = 10\gamma$ and $\Delta_c = \Delta_p = 0$. Other used parameters are $M = 7$, $L = 30$, and $R = 4$.

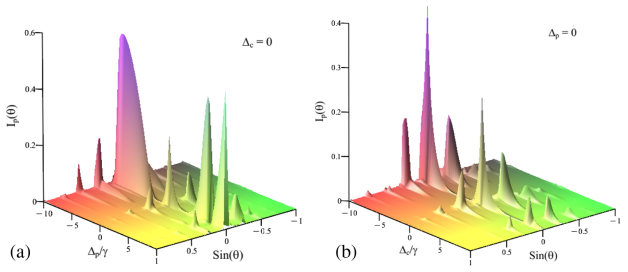

Fig. 4. Diffraction pattern (a) as a function of sin θ and the probe detuning Δ_p when the coupling detuning $\Delta_c = 0$ or (b) as a function of sin θ and the coupling detuning Δ_c when the probe detuning $\Delta_p = 0$. Other used parameters are $M = 7$, $L = 30$, $R = 4$, $\Omega_c = 10\gamma$, and $\Omega_p = 0.8\gamma$.

patterns as a function of sin θ and the probe detuning Δ_p when the coupling detuning $\Delta_c = 0$ [Fig. 4(a)] or a function of sin θ and the coupling detuning Δ_c when the probe detuning $\Delta_p = 0$ [Fig. 4(b)]. In Fig. 4(a), by fixing the coupling detuning at $\Delta_c = 0$ we can easily observe the three diffraction patterns with different orders at three EIT windows: $\Delta_p = 0$, $\Delta_p = -9\gamma$, and $\Delta_p = 7.6\gamma$. At the same time, at these frequency regions the intensity of zero-order diffraction is extraordinarily increased due to the EIT effect being established. In addition, we also note that because of small absorption in regions far from the resonance frequency (outside the EIT windows), zero-order diffraction can still occur. In Fig. 4(b), at the given probe frequency ($\Delta_p = 0$), the diffraction pattern at this probe frequency also occurs only when the coupling frequency detuning is $\Delta_c = 0$, $\Delta_c = -9\gamma$, and $\Delta_c = 7.6\gamma$ corresponding to the two-photon resonance condition for the EIT formation of the probe field as shown in Ref. [24].

To further illustrate MEIG, in Fig. 4(a), we plot the diffraction patterns as a function of sinθ at different probe detunings $\Delta_p = 0$, $\Delta_p = -9\gamma$, and $\Delta_p = 7.6\gamma$ as shown in Figs. 5(a)–5(c). Again we see that at these probe frequencies the diffraction pattern appears with different orders of diffraction. However, because the transparency depths at the EIT windows are not

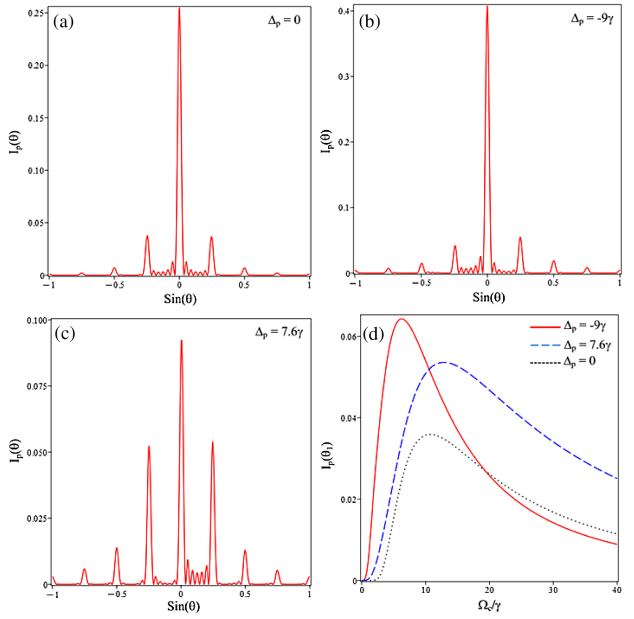

Fig. 5. Fixed coupling frequency detuning at $\Delta_c = 0$ and $\Omega_c = 10\gamma$. MEIG occurs simultaneously at different probe frequency detunings: (a) $\Delta_p = 0$, (b) $\Delta_p = -9\gamma$, and (c) $\Delta_p = 7.6\gamma$. (d) Variations of the first-order diffraction intensities versus the coupling intensity Ω_c at the probe frequency detuning corresponding to (a)–(c). Other used parameters are $M = 7$, $L = 30$, $R = 4$, and $\Omega_p = 0.8\gamma$.

the same (see Fig. 2), the diffraction efficiencies are also different. For example, the zero-order diffraction efficiency at the probe frequency $\Delta_p = -9\gamma$ is the best while at $\Delta_p = 7.6\gamma$ it is the worst. This is completely consistent with the fact that because the relative coupling strengths between the transitions $|2\rangle \leftrightarrow |3\rangle$, $|2\rangle \leftrightarrow |4\rangle$, and $|2\rangle \leftrightarrow |5\rangle$ are 1:1.46:0.6, the EIT window at $\Delta_p = -9\gamma$ corresponding to the coupling transition $|2\rangle \leftrightarrow |4\rangle$ has the best transparency depth, while at $\Delta_p = 7.6\gamma$ corresponding to the coupling transition $|2\rangle \leftrightarrow |5\rangle$, the transparency depth is the weakest. Figure 5(d) displays the first-order diffraction intensity as a function of coupling intensity Ω_c at different probe detunings corresponding to Figs. 5(a)–5(c). It is easy to observe that the first-order diffraction intensities at different EIT windows are also different and they vary strongly with the coupling intensity Ω_c. This investigation allows us to find the optimal value of Ω_c to obtain the best first-order diffraction efficiency at each EIT window. For example, the first-order diffraction intensity at $\Delta_p = 0$, $\Delta_p = -9\gamma$, and $\Delta_p = 7.6\gamma$ reaches its maximum value when $\Omega_c = 11\gamma$, $\Omega_c = 6.5\gamma$, and $\Omega_c = 13\gamma$, respectively.

Figure 6 presents a similar investigation as in Fig. 5 but here the diffraction patterns of the probe field are plotted at different coupling detunings $\Delta_c = 0$, $\Delta_c = -9\gamma$, and $\Delta_c = 7.6\gamma$ when the probe detuning is fixed at $\Delta_p = 0$, corresponding to Fig. 4(b). From Figs. 6(a)–6(c), we can see that when adjusting the frequency of the coupling field around the transition $|2\rangle \leftrightarrow |3\rangle$, we can find three values of coupling frequency to have the diffraction pattern of the probe field with different orders of diffraction. Similar to Fig. 5, the best diffraction efficiency corresponds to $\Delta_c = -9\gamma$ and the worst diffraction efficiency corresponds to $\Delta_c = 7.6\gamma$. Figure 6(c) depicts the

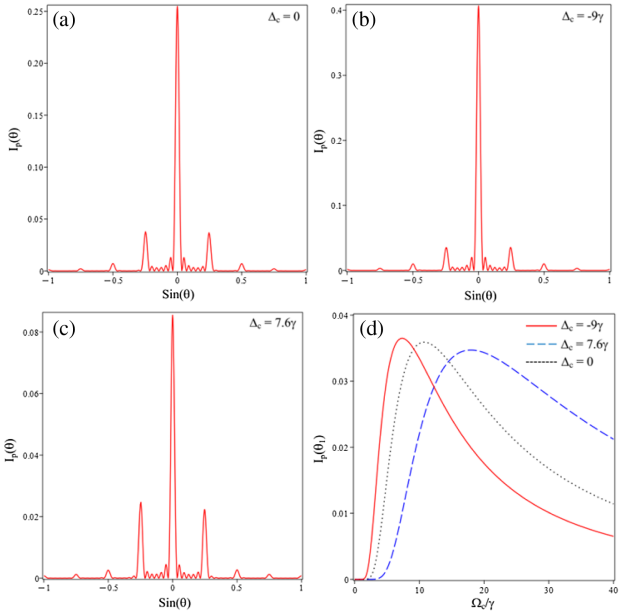

Fig. 6. Fixed probe frequency detuning at $\Delta_p = 0$ and $\Omega_c = 10\gamma$. EIG for the probe beam occurs when the coupling beam frequency is satisfied as (a) $\Delta_c = 0$, (b) $\Delta_c = -9\gamma$, and (c) $\Delta_c = 7.6\gamma$. (d) Variations of the first-order diffraction intensities versus the coupling intensity Ω_c at the coupling frequency detuning corresponding to (a)–(c). Other used parameters are $M = 7$, $L = 30$, $R = 4$, and $\Omega_p = 0.8\gamma$.

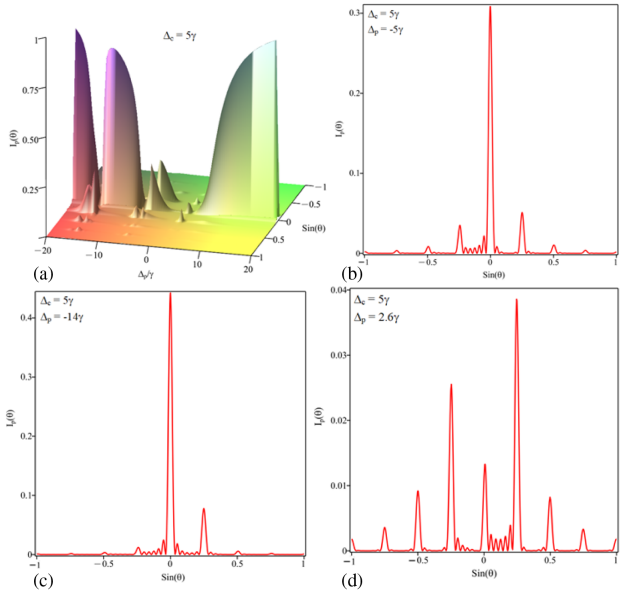

Fig. 7. (a) Diffraction pattern as a function of $\sin\theta$ and the probe detuning Δ_p when the coupling detuning $\Delta_c = 5\gamma$. Fixed coupling frequency detuning at $\Delta_c = 5\gamma$. MEIG occurs simultaneously at different probe detunings: (b) $\Delta_p = -5\gamma$, (c) $\Delta_p = -14\gamma$, and (d) $\Delta_p = 2.6\gamma$. Other used parameters are $M = 7$, $L = 30$, $R = 4$, $\Omega_c = 10\gamma$, and $\Omega_p = 0.8\gamma$.

variations of first-order diffraction intensities versus the coupling intensity Ω_c at different coupling detunings $\Delta_c = 0$, $\Delta_c = -9\gamma$, and $\Delta_c = 7.6\gamma$. In this case, the first-order diffraction intensity at $\Delta_c = 0$, $\Delta_c = -9\gamma$, and $\Delta_c = 7.6\gamma$ reaches its maximum value when $\Omega_c = 11\gamma$, $\Omega_c = 6.5\gamma$, and $\Omega_c = 18\gamma$, respectively.

In addition, by changing the coupling laser frequency, we can also find MEIG at the desired probe laser frequencies. For example, in Fig. 7(a), we choose the coupling laser frequency as $\Delta_c = 5\gamma$, and plot the three-dimensional diffraction pattern as a function of $\sin\theta$ and the probe detuning Δ_p. In this case MEIG occurs at probe frequencies that satisfy the two-photon resonance condition, specifically $\Delta_p = -\Delta_c = -5\gamma$, $\Delta_p = -\Delta_c - \delta_1 = -14\gamma$, and $\Delta_p = -\Delta_c + \delta_2 = 2.6\gamma$. In more detail, we describe the diffraction pattern at the indicated probe frequency detunings, as shown in Figs. 7(b)–7(d).

In Fig. 8, we investigate the variations of zero-, first-, and second-order diffraction intensities according to probe detuning [Fig. 8(a)] and coupling detuning [Fig. 8(b)] when the coupling intensity is fixed at $\Omega_c = 10\gamma$. From Fig. 8(a), we can easily observe that the zero-, first-, and second-order diffraction intensities of EIG are mainly distributed simultaneously in three probe frequency regions $\Delta_p = 0$, $\Delta_p = -9\gamma$, and $\Delta_p = 7.6\gamma$ corresponding to three EIT windows. Furthermore, we can also estimate that the maximum first-order diffraction efficiency can be achieved at about 23% (dashed line). Similarly, in Fig. 8(b), the zero-, first-, and second-order diffraction intensities are mainly distributed in the three coupling frequency regions $\Delta_c = 0$, $\Delta_c = -9\gamma$, and $\Delta_c = 7.6\gamma$, and the maximum first-order diffraction efficiency can be achieved at about 19% (dashed line). Thus, by fixing one of the two laser fields,

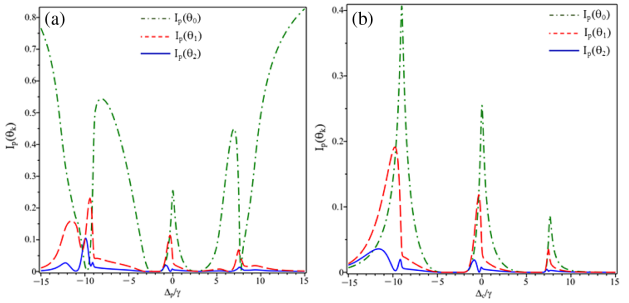

Fig. 8. Variation of the k-order diffraction intensity $I_p(\theta_k)$ (a) as a function of the probe detuning Δ_p when the coupling detuning $\Delta_c = 0$ or (b) as a function of the coupling detuning Δ_c when the probe detuning $\Delta_p = 0$. Other used parameters are $M = 7$, $L = 30$, $R = 4$, $\Omega_c = 10\gamma$, and $\Omega_p = 0.8\gamma$.

and adjusting the frequency of the other laser field around the atomic resonance frequency, we can simultaneously obtain probe diffraction patterns with different orders of diffraction at three frequency regions.

In Fig. 9, we examine the influence of interaction length on first-order diffraction efficiency at three different frequency regions of the probe beam [Fig. 9(a)] or the coupling beam [Fig. 9(b)]. The curves show that the first-order diffraction intensity depends sensitively on the interaction length L of the atomic sample. For small values of L, the first-order diffraction intensity increases linearly with L and reaches its maximum value, and then the diffraction intensity decreases when L is large enough. In addition, the value of L for which the maximum first-order diffraction intensity is different for different probe and coupling frequencies.

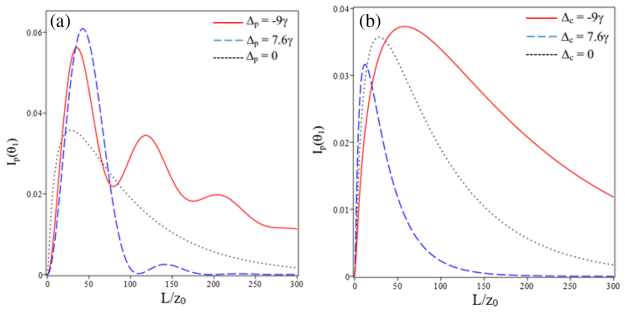

Fig. 9. Variations of the first-order diffraction intensity $I_p(\theta_1)$ as a function of the interaction length L (a) when the coupling detuning $\Delta_c = 0$ or (b) when the probe detuning $\Delta_p = 0$. Other used parameters are $M = 7$, $L = 30$, $R = 4$, $\Omega_c = 10\gamma$, and $\Omega_p = 0.8\gamma$.

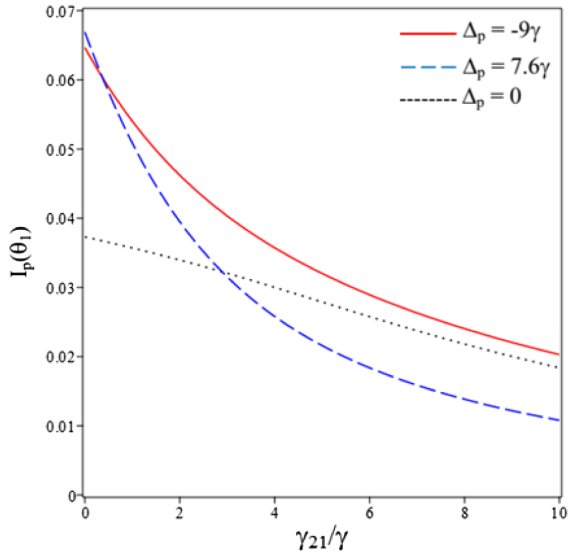

Fig. 10. Variations of the first-order diffraction intensity $I_p(\theta_1)$ as a function of the decay rate γ_{21} when the coupling detuning $\Delta_c = 0$. Other used parameters are $M = 7$, $L = 30$, $R = 4$, $\Omega_c = 10\gamma$, and $\Omega_p = 0.8\gamma$.

In fact, our theoretical model is perfectly applicable to any atomic/molecular system when the frequency gap between the superfine states is of the order of laser beam width. Each atom/molecular system with each used state has different decay rates, and the interference and diffraction phenomena are strongly dependent on the atomic decay rate. To see this dependence, therefore, in Fig. 10 we plot the variation of first-order diffraction intensity according to the decay rate of the level $|2\rangle$ at the probe detunings $\Delta_p = 0$, $\Delta_p = -9\gamma$, and $\Delta_p = 7.6\gamma$. The graphs constructed at the parameters of the coupling laser field are $\Delta_c = 0$ and $\Omega_c = 10\gamma$. It shows that when the used states in the excited configuration have a smaller decay rate, the interference and diffraction phenomena are produced with better efficiency and vice versa. This is also one reason why EIG is difficult to perform with a hot atomic gas medium subject to large Doppler width.

4. CONCLUSION

We have studied the generation of a multiple electromagnetically induced grating based on multiple electromagnetically induced transparency in the five-level ladder-type scheme of the ^{85}Rb atom excited by a probe laser field and only one coupling laser field. The diffraction pattern of the probe field on the atomic sample is observed at three different frequency regions corresponding to three EIT windows of the system. Likewise, we also found three different frequency regions of the coupling field satisfying the two-photon resonance condition to obtain the diffraction pattern of the probe field at a given frequency. In addition, the multiple electromagnetically induced grating can also be formed at desired probe frequencies when changing the coupling laser frequency to satisfy the two-photon resonance condition. By varying the coupling intensity or frequency detuning, the high-order diffraction efficiency can be improved and optimized.

Funding. Bộ Giáo dục và Đào tạo (B2023-TDV-08).

Disclosures. The authors declare no conflicts of interest.

Data availability. The data that support the findings of this study are available upon request from the corresponding author.

REFERENCES

1. K. J. Boller, A. Imamoglu, and S. E. Harris, "Observation of electromagnetically induced transparency," Phys. Rev. Lett. **66**, 2593–2596 (1991).
2. N. H. Bang, L. V. Doai, and D. X. Khoa, "Controllable optical properties of multiple electromagnetically induced transparency in gaseous atomic media," Commun. Phys. **28**, 1–33 (2019).
3. A. Lezama, S. Barreiro, and A. M. Akulshin, "Electromagnetically induced absorption," Phys. Rev. A **59**, 4732–4735 (1999).
4. A. S. Zibrov, M. D. Lukin, D. E. Nikonov, *et al.*, "Experimental observation of laser oscillation without population inversion via quantum interference in Rb," Phys. Rev. Lett. **75**, 1499–1502 (1995).
5. H. Schmidt and A. Imamoglu, "Giant Kerr nonlinearities obtained by electromagnetically induced transparency," Opt. Lett. **21**, 1936–1938 (1996).
6. H. Kang and Y. Zhu, "Observation of large Kerr nonlinearity at low light intensities," Phys. Rev. Lett. **91**, 093601 (2003).
7. A. Joshi, A. Brown, H. Wang, *et al.*, "Controlling optical bistability in a three-level atomic system," Phys. Rev. A **67**, 041801(R) (2003).
8. L. V. Hau, S. E. Harris, Z. Dutton, *et al.*, "Light speed reduction to 17 metres per second in an ultracold atomic gas," Nature **397**, 594–598 (1999).
9. D. F. Phillips, A. Fleischhauer, A. Mair, *et al.*, "Storage of light atom vapor," Phys. Rev. Lett. **86**, 783–786 (2001).
10. G. Huang, K. Jiang, M. G. Payne, *et al.*, "Formation and propagation of coupled ultraslow optical soliton pairs in a cold three-state double-lambda system," Phys. Rev. E **73**, 056606 (2006).
11. A. Fountoulakis, A. F. Terzis, and E. Paspalakis, "All-optical modulation based on electromagnetically induced transparency," Phys. Lett. A **374**, 3354–3364 (2010).
12. H. Ling, Y.-Q. Li, and M. Xiao, "Electromagnetically induced grating: homogeneously broadened medium," Phys. Rev. A **57**, 1338–1344 (1998).
13. M. Mitsunaga and N. Imoto, "Observation of an electromagnetically induced grating in cold sodium atoms," Phys. Rev. A **59**, 4773–4776 (1999).
14. Y. Chen, X. G. Wei, and B. S. Ham, "Optical properties of an N-type system in Doppler-broadened multilevel atomic media of the rubidium D2 line," J. Phys. B **42**, 065506 (2009).
15. J. Qi, "Electromagnetically induced transparency in an inverted Y-type four-level system," Phys. Scr. **81**, 015402 (2009).

16. S. Li, X. Yang, X. Cao, *et al.*, "Two electromagnetically induced transparency windows and an enhanced electromagnetically induced transparency signal in a four-level tripod atomic system," J. Phys. B **40**, 3211–3219 (2007).
17. D. Han, Y. Zeng, Y. Bai, *et al.*, "Controlling the group velocity in a five-level K-type atomic system," Opt. Comm. **281**, 4712–4714 (2008).
18. Y. Hong, Y. Dong, Z. Mei, *et al.*, "Absorption and dispersion control in a five-level M-type atomic system," Chin. Phys. B **21**, 114207 (2012).
19. E. Paspalakis and P. L. Knight, "Electromagnetically induced transparency and controlled group velocity in a multilevel system," Phys. Rev. A **66**, 015802 (2002).
20. H. R. Hamedi and G. Juzeliunas, "Phase-sensitive Kerr nonlinearity for closed-loop quantum systems," Phys. Rev. A **91**, 053823 (2015).
21. H. Jafarzadeh, "Controlling the optical bistability in a multi-level atomic system via similar parameters of quantum well nanostructure," J. Appl. Phys. **117**, 163103 (2015).
22. Y. Li, C. Hang, L. Ma, *et al.*, "Controllable entanglement of lights in a five-level system," Phys. Lett. A **354**, 1–7 (2006).
23. J. Wang, L. B. Kong, X. H. Tu, *et al.*, "Electromagnetically induced transparency in multi-level cascade scheme of cold rubidium atoms," Phys. Lett. A **328**, 437–443 (2004).
24. L. V. Doai, P. V. Trong, D. X. Khoa, *et al.*, "Electromagnetically induced transparency in five-level cascade scheme of ^{85}Rb atoms: an analytical approach," Optik **125**, 3666–3669 (2014).
25. N. T. Anh, L. V. Doai, and N. H. Bang, "Manipulating multi-frequency light in a five-level cascade-type atomic medium associated with giant self-Kerr nonlinearity," J. Opt. Soc. Am. B **35**, 1233–1239 (2018).
26. D. X. Khoa, L. V. Doai, D. H. Son, *et al.*, "Enhancement of self-Kerr nonlinearity via electromagnetically induced transparency in a five-level cascade system: an analytical approach," J. Opt. Soc. Am. B. **31**, 1330–1334 (2014).
27. D. X. Khoa, L. V. Doai, L. N. M. Anh, *et al.*, "Optical bistability in a five-level cascade EIT medium: an analytical approach," J. Opt. Soc. Am. B **33**, 735–740 (2016).
28. G. Cardoso and J. Tabosa, "Electromagnetically induced gratings in a degenerate open two-level system," Phys. Rev. A **65**, 033803 (2002).
29. B. K. Dutta and P. K. Mahapatra, "Electromagnetically induced grating in a three-level X-type system driven by a strong standing wave pump and weak probe fields," J. Phys. B **39**, 1145–1157 (2006).
30. S. A. Carvalho and L. E. E. de Araujo, "Electromagnetically induced blazed grating at low light levels," Phys. Rev. A **83**, 053825 (2011).
31. S. Asghar, S. Qamar, and S. Qamar, "Electromagnetically induced grating with Rydberg atoms," Phys. Rev. A **94**, 033823 (2016).
32. T. Naseri, "Optical properties and electromagnetically induced grating in a hybrid semiconductor quantum dot-metallic nanorod system," Phys. Lett. A **384**, 126164 (2020).
33. J. W. Tabosa, A. Lezama, and G. Cardoso, "Transient Bragg diffraction by a transferred population grating: application for cold atoms velocimetry," Opt. Commun. **165**, 59–64 (1999).
34. P. W. Zhai, X. M. Su, and J. Y. Gao, "Optical bistability in electromagnetically induced grating," Phys. Lett. A **289**, 27–33 (2001).
35. A. W. Brown and M. Xiao, "All-optical switching and routing based on an electromagnetically induced absorption grating," Opt. Lett. **30**, 699–701 (2005).
36. D. Moretti, D. Felinto, and J. W. R. Tabosa, "Dynamics of a stored Zeeman coherence grating in an external magnetic field," J. Phys. B **43**, 115502 (2010).
37. L. Zhao, W. Duan, and S. F. Yelin, "All-optical beam control with high speed using image-induced blazed gratings in coherent media," Phys. Rev. A **82**, 013809 (2010).
38. J. Wen, Y. H. Zhai, S. Du, *et al.*, "Engineering biphoton wave packets with an electromagnetically induced grating," Phys. Rev. A **82**, 043814 (2010).
39. F. Zhou, Y. Qi, H. Sun, *et al.*, "Electromagnetically induced grating in asymmetric quantum wells via Fano interference," Opt. Express **21**, 12249–12259 (2013).
40. Y. Zhang, Z. Wu, X. Yao, *et al.*, "Controlling multi-wave mixing signals via photonic band gap of electromagnetically induced absorption grating in atomic media," Opt. Express **21**, 29338–29349 (2013).
41. T. Qiu and G. Yang, "Electromagnetically induced angular Talbot effect," J. Phys. B **48**, 245502 (2015).
42. G. Solookinejad, M. Panahi, E. A. Sangachin, *et al.*, "Plasmonic structure induced giant Goos-Hänchen shifts in a four-level quantum system," Chin. J. Phys. **54**, 651–658 (2016).
43. Z. H. Xiao, S. G. Shin, and K. Kim, "An electromagnetically induced grating by microwave modulation," J. Phys. B **43**, 161004 (2010).
44. R. Sadighi-Bonabi, T. Naseri, and M. Navadeh-Toupchi, "Electromagnetically induced grating in the microwavedriven four-level atomic systems," Appl. Opt. **54**, 368–377 (2015).
45. N. Ba, X.-Y. Wu, X.-J. Liu, *et al.*, "Electromagnetically induced grating in an atomic system with a static magnetic field," Opt. Commun. **285**, 3792–3797 (2012).
46. T. Naseri and R. Sadighi-Bonabi, "Electromagnetically induced phase grating via population trapping condition in a microwave-driven four-level atomic system," J. Opt. Soc. Am. B **31**, 2879–2884 (2014).
47. N. Ba, L. Wang, X.-Y. Wu, *et al.*, "Electromagnetically induced grating based on the giant Kerr nonlinearity controlled by spontaneously generated coherence," Appl. Opt. **52**, 4264–4272 (2013).
48. A. Hussain, M. Abbas, and H. Ali, "Electromagnetically induced grating via Kerr nonlinearity, Doppler broadening and spontaneously generated coherence," Phys. Scr. **96**, 125110 (2021).
49. T. Naseri and R. Sadighi-Bonabi, "Efficient electromagnetically induced phase grating via quantum interference in a four-level N-type atomic system," J. Opt. Soc. Am. B **31**, 2430–2437 (2014).
50. L. Zhao, "Electromagnetically induced polarization grating," Sci. Rep. **8**, 3073 (2018).
51. A. Vafafard and M. Sahrai, "Tunable double electromagnetically induced grating with an incoherent pump field," J. Opt. Soc. Am. B **37**, 244–250 (2020).
52. D. McGloin, D. J. Fullton, and M. H. Dunn, "Electromagnetically induced transparency in N-level cascade schemes," Opt. Commun. **190**, 221–229 (2001).